The Role of Closed Gyres in Setting the Zonal Transport of the Antarctic Circumpolar Current

LOUIS-PHILIPPE NADEAU AND RAFFAELE FERRARI

Department of Earth, Atmospheric, and Planetary Sciences, Massachusetts Institute of Technology, Cambridge, Massachusetts

(Manuscript received 22 August 2014, in final form 22 January 2015)

ABSTRACT

Eddy-permitting simulations are used to show that basinlike gyres can be observed in the large-scale barotropic flow of a wind-driven channel with a meridional topographic ridge. This is confirmed using both two-layer quasigeostrophic and 25-level primitive equation models at high horizontal resolution. Comparing results from simulations with and without the topographic ridge, it is shown that the zonal baroclinic transport in the channel increases with increasing wind stress when the bottom topography is flat but not when there is a meridional ridge. The saturation of transport for increasing wind occurs in conjunction with the development of recirculating gyres in the large-scale barotropic streamfunction. This suggests that the total circulation can be thought of as a superposition of a gyre mode (which has zero circumpolar transport) and a free circumpolar mode (which contains all of the transport). Basinlike gyres arise in the channel because the topography steers the barotropic streamlines and supports a frictional boundary layer similar to the more familiar ones observed along western boundaries. The gyre mode is thus closely linked with the bottom form stress exerted by the along-ridge flow and provides the sink for the wind momentum input. In this framework, any increase in wind forcing spins a stronger gyre as opposed to feeding the circumpolar transport. This hypothesis is supported with a suite of experiments where key parameters are carried over a wide range: wind stress, wind stress curl, ridge height, channel length, and bottom friction.

1. Introduction

The Antarctic Circumpolar Current (ACC) flows uninterrupted around Antarctica and mixes together Atlantic, Indian, and Pacific Ocean waters. It is the most voluminous ocean current with a transport in excess of 130 Sverdrups (Sv; $1\,\text{Sv} \equiv 10^6\,\text{m}^3\,\text{s}^{-1}$) (Firing et al. 2011). Despite its global importance, we still lack a robust quantitative theory for what sets the magnitude of this transport. The early works of Stommel (1957) and Gill (1968) focused on the role of topography and on the connection to the ocean basins to the north. Over the last 20 years, it has become clear that geostrophic eddies are an additional crucial aspect of ACC dynamics (Marshall and Speer 2012), but we are still far from having a theory of the ACC transport as complete as Sverdrup's theory for the transport of the western boundary currents along continental margins (Pedlosky 1996).

The emerging consensus is that the ACC vertically integrated zonal transport is set by a balance of three terms in the time-averaged zonal momentum budget: (i) the input of momentum by the wind exerted at the ocean surface, (ii) the downward transport of momentum by geostrophic eddies, and (iii) the sink of momentum exerted by topographic form drag at the ocean bottom (Munk and Palmen 1951). Numerical simulations further show that topography prevents the development of a strong abyssal circumpolar flow (e.g., Ward and Hogg 2011; Firing et al. 2011) so that most of the transport is confined to the upper half of the water column. This led a number of recent studies to argue that the circumpolar transport can be understood as a balance between the wind stress and geostrophic eddies, the two forces that dominate in the upper ocean (Johnson and Bryden 1989). This balance has been invoked to explain the numerical evidence that, in eddy-resolving models of

Corresponding author address: Louis-Philippe Nadeau, Department of Earth, Atmospheric, and Planetary Sciences, 54-1622, Massachusetts Institute of Technology, 77 Massachusetts Ave. Cambridge, MA 02139-4307.
E-mail: lpnadeau@mit.edu

DOI: 10.1175/JPO-D-14-0173.1

wind-driven reentrant channels, the transport does not increase much with increasing surface winds (e.g., Hallberg and Gnanadesikan 2006; Meredith et al. 2012; Munday et al. 2013; Morrison and Hogg 2013). The argument is that as the wind stress increases, the mean flow in the channel increases and becomes more unstable, thus generating stronger eddies. The eddies build up over a few years until a new equilibrium is achieved where the eddies offset much of the effect of increasing the winds, curbing the increase in the along-channel transport, a limit referred to as "eddy saturation" (Straub 1993). The implicit assumption is that the topographic drag is slaved to balance the downward eddy transport of momentum and does not exert an active control on the channel transport.

Thompson and Naveira Garabato (2014) and Abernathey and Cessi (2014) challenged this view and argued that topographic ridges control the overall ACC transport by modifying the characteristics of the geostrophic eddies. They argued that in flat bottom channels, the geostrophic eddies are transient features generated through baroclinic instabilities, while in the presence of uneven topography the geostrophic eddy field is dominated by large-scale meanders in the lee of the major ridges. Importantly, the meanders result in a substantial topographic form drag over the ridges. In this view, the ACC transport's insensitivity to increase in wind forcing was interpreted as the localized increase in topographic form drag.

Nadeau and Straub (2009, 2012) and Nadeau et al. (2013) (hereinafter NS09, NS12, and NSH13) proposed that the effect of topography on the ACC transport is better thought of as a global constraint coupling the channel flow to the gyre flows in closed basins to the north rather than a localized effect at meanders. They suggested decomposing the total transport into a basin and a channel contribution. They found that as the wind increased, the channel transport did not increase. Instead, a closed recirculating gyre developed that expanded from the basin into the channel. In their analytic model, the saturation of transport depended crucially on the presence of a basin region to the north. The argument, however, is not complete because saturation has been reported in channels without basins to the north.

In this manuscript, we show that closed recirculating gyres develop in the lee of major topographic ridges, regardless of the presence of a basin to the north. The gyre circulations increase with the wind stress without any increase in the along-channel transport. Our main result is illustrated in Fig. 1, which shows the circulations that develop in a two-layer quasigeostrophic model in basin and channel geometries. The model is forced with a zonal eastward wind that vanishes at the north and south boundaries and peaks in the center of the domain. The model is described in detail in the next section. The upper panels of Fig. 1 show the barotropic streamfunctions, that is, the streamfunctions associated with the vertically integrated horizontal flow in a closed-box geometry with a semi-Gaussian continental shelf along the meridional boundaries, hereinafter referred to as Box+Ridge. The circulation is composed of two counterrotating gyres both for weak (left panel) and strong (right panel) winds in agreement with Sverdrup's theory (Pedlosky 1996). The middle panels, labeled Channel+Ridge, show the same two experiments but without the meridional walls, resulting in a reentrant channel with a Gaussian ridge at the origin (equal to the continental shelf in the previous experiments). The bottom panels, labeled Channel+Flat, show reentrant channel simulations where the bottom topography has been flattened. For weak wind forcing, the Channel+Ridge simulation behaves like a flat bottom channel. However, for strong wind forcing, it develops a basinlike double-gyre circulation. This result is rather counterintuitive since there is no lateral boundary to support a western boundary current. The main goal of this manuscript is to understand the transition from channel-like flow to basin-like flow for increasing wind forcing in channel simulations with ridges and explain how this affects the channel transport.

Section 2 introduces the quasigeostrophic and primitive equation numerical simulations used in the study. Section 3 analyzes the numerical results and shows that the channel flow can be thought of as a combination of a purely zonal circumpolar flow and a closed gyre recirculation, which does not contribute any zonally averaged transport. The gyre affects the momentum balance such that the channel transport is independent of the wind forcing. Section 4 tests the robustness of this hypothesis by varying four key parameters: the height of the topographic ridge, the channel length, the wind stress curl, and the bottom friction. We compare our results to earlier work in section 5 and provide conclusions in section 6.

2. Numerical models and experiment design

a. *Quasigeostrophic model*

The quasigeostrophic (QG) simulations are performed using the same numerical model described in the appendix and NS09. The model solves the two-layer quasigeostrophic potential vorticity equation on a β plane. The thicknesses of the upper and lower layers are $H_1 = 1200\,\text{m}$ and $H_2 = 2800\,\text{m}$, respectively. In the reference simulation, the model geometry is a 4-km-deep reentrant channel, $L_x = 9600\,\text{km}$ long, and $L_y = 3840\,\text{km}$ wide, with an h_0 high meridional Gaussian ridge

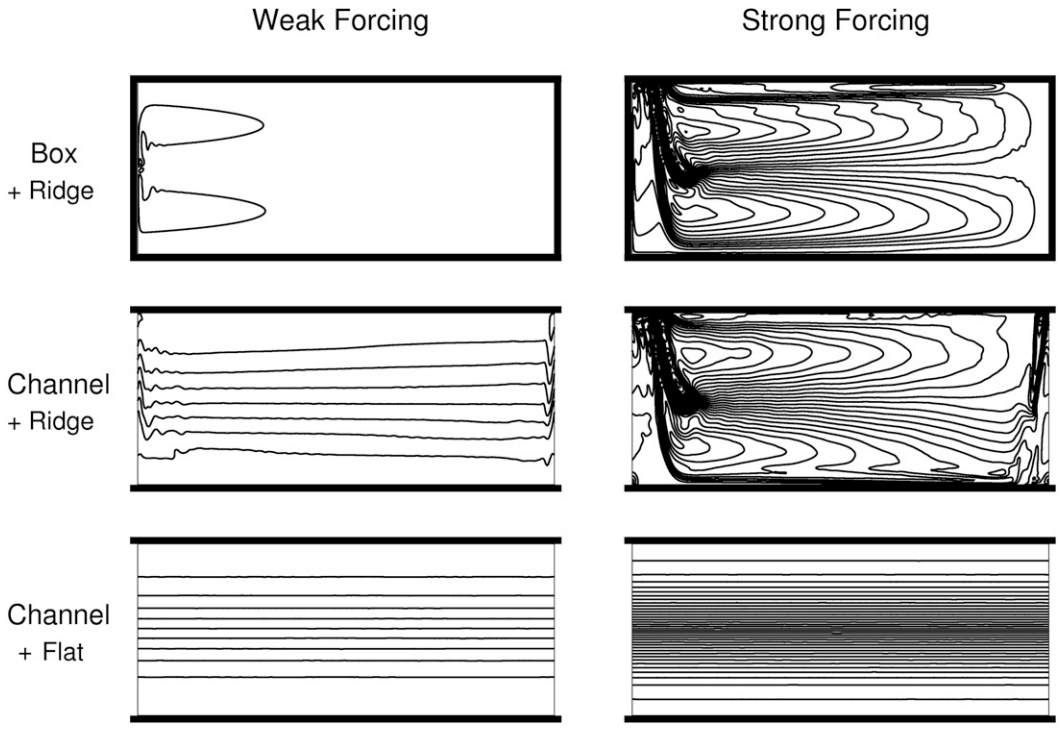

FIG. 1. Time-mean barotropic streamfunction from (left) weak and (right) strong wind forcing for three different basin setups: (top) the classical double gyre in a closed-box geometry with semi-Gaussian continental shelves (Box+Ridge), (middle) as in Box+Ridge but without meridional walls (Channel+Ridge), and (bottom) as in Channel+Ridge but without topography (Channel+Flat). The Rossby radius of deformation is 24 km. The wind stress amplitude is $\tau_0 = 0.02\,\mathrm{N\,m^{-2}}$ in the weak forcing case and $0.4\,\mathrm{N\,m^{-2}}$ in the strong forcing case. Each streamline equals 15 Sv in the four upper panels. This scale becomes 75 Sv in the lower-left panel and 300 Sv in the lower-right panel.

topography centered at the longitude $x = 0$ (or equivalently $x = L_x$):

$$h_b = h_0 \exp\left[-\frac{(x_0 - x)^2}{2\sigma^2}\right], \tag{1}$$

with $\sigma = 340$ km. Some experiments are performed in a closed-box ocean, in which case a vertical wall is added on top of the ridge at its maximum height: $x = 0$ and $x = L_x$. In this closed-box geometry, the ridge represents western and eastern continental shelves. The ridge shelf is set to $h_0 = 2$ km in the reference simulation and never so high as to completely block the deeper layer.

The channel is forced at the surface with a wind stress. In the reference case, the wind stress profile is given by

$$\boldsymbol{\tau} = \tau_0 \sin^2(\pi y/L_y)\mathbf{i}. \tag{2}$$

A linear drag, with $r = 10^{-7}\,\mathrm{s^{-1}}$, is applied at the bottom. Biharmonic dissipation, with $A_h = 10^{10}\,\mathrm{m^4\,s^{-1}}$, is applied in both layers. No normal flow and free-slip conditions ($\nabla^2\psi = 0$) are imposed at lateral walls. In addition, the condition $\nabla^4\psi = 0$ is also added to ensure that the biharmonic dissipation does not generate energy at the solid walls. We use a third-order Adams–Bashforth scheme for time derivatives, center differencing in space with a horizontal resolution of 15 km, an Arakawa (1966) scheme for the Jacobian, and a multigrid method for the elliptic inversions.

The external Rossby deformation radius is defined as $L_B = \sqrt{gH}/f_0 = 1525$ km, where g is the gravitational acceleration, H is the total ocean depth, and f_0 is the Coriolis parameter. The internal deformation radius is defined as $L_\rho = \sqrt{(g' H_1 H_2)/H}/f_0$, where g' is the reduced gravity. By varying the value of the reduced gravity, we perform QG experiments for four internal deformation radii: $L_\rho = 24, 32, 40$, and 48 km. Thus, in all simulations the Gaussian ridge is much wider than the internal deformation radius. A summary of the model parameters for all QG simulations is given in Table 1.

b. Primitive equation model

A few primitive equation (PE) model runs are performed to support the key QG results. The model code is the hydrostatic version of the MITgcm (Marshall et al.

TABLE 1. Model parameters for the reference quasigeostrophic simulations.

Parameter	Value
First Rossby deformation radius	$L_\rho = 24$, 32, 40 and 48 km
Horizontal resolution	$\Delta x = \Delta y = 15$ km
Length of channel	$L_x = 9600$ km
Width of channel	$L_y = 3840$ km
Latitude where $\text{curl}_z(\tau) = 0$	$L_y/2 = 1920$ km
Depth of upper layer	$H_1 = 1200$ m
Depth of bottom layer	$H_2 = 2800$ m
Height of Gaussian ridge	$H_0 = 2000$ m
Coriolis parameter	$f_0 = -1.3 \times 10^{-4}\,\text{s}^{-1}$
Beta parameter	$\beta = 1.5 \times 10^{-11}\,\text{m}^{-1}\,\text{s}^{-1}$
Reference density	$\rho_1 = 1035\,\text{kg m}^{-3}$
Bottom friction coefficient	$r = 10^{-7}\,\text{s}^{-1}$
Biharmonic dissipation coefficient	$A_h = \beta \times \Delta x^5$

1997a,b). The domain is a Cartesian grid similar to that used for the QG model but with a 10-km horizontal resolution and 25 vertical levels and thickness increasing from 60 m at the surface to 210 m at the bottom. Dissipation of momentum is through a biharmonic operator with a hyperviscosity $A_h = 1.7 \times 10^{10}\,\text{m}^4\,\text{s}^{-1}$ together with a Leith scheme viscosity (Leith 1967). In the reference case, a linear bottom drag coefficient $r = 2.8 \times 10^{-4}\,\text{s}^{-1}$ acts on the bottom level.[1] A buoyancy diffusivity $\kappa_\nu = 5 \times 10^{-6}\,\text{m}^2\,\text{s}^{-1}$ is applied in the vertical, whereas no buoyancy diffusivity is applied in the horizontal; in this limit, diffusion of buoyancy is likely dominated by the numerical discretization, consistent with our goal to keep diffusion as small as numerically feasible. Ocean convection is parameterized with implicit vertical diffusion. Advection of buoyancy is achieved through the second-order moment scheme of Prather (1986), which minimizes numerical mixing of buoyancy (Hill et al. 2012).

To keep the experiments as consistent as possible with the QG simulations, the flow is forced with the same surface wind stress and no buoyancy flux. Stratification is initialized to a horizontally uniform exponential vertical profile with an e-folding scale such that the first deformation radius equals that of the corresponding QG simulation. More specifically, the initial temperature field takes the form $T = T_0 e^{z/z_d}$, where z_d is the e-folding scale and T_0 is the surface temperature. We use a linear equation of state with a thermal expansion coefficient $\alpha = 2 \times 10^{-4}\,\text{K}^{-1}$. The first Rossby radius L_ρ is obtained solving a Sturm–Liouville eigenvalue problem and is given by the smallest zeros of $J_1[(N_0 z_d)/L_\rho] - [g/(N_0 L)]J_0[(N_0 z_d)/L_\rho] = 0$ (Wunsch and Gill 1976), where J_0 and J_1 are Bessel functions, and $N = \sqrt{-(g/\rho_0)(\partial\rho/\partial z)} = N_0 e^{z/2z_d}$ is the stratification.

Without surface buoyancy fluxes, one could expect to lose the initial stratification before the winds and eddies reach an equilibrium. However, the slope of the density surfaces reaches a statistical equilibrium after 200 yr for all simulations. The equilibrium stratification varies from north to south, but the globally averaged first Rossby radius remains close to that set by the initial stratification. Model diagnostics are computed over 200 yr after the model has reached statistical equilibrium and before vertical mixing starts eroding away the interior stratification.

c. Diagnostics

Throughout this manuscript, the baroclinic transport is defined as the zonal average of $T_{\text{BC}} = \int_{-H}^{0}\int_{0}^{L_y}[u(z) - u_{\text{bottom}}]\,dy\,dz$, whereas the barotropic transport is defined as the zonal average of the total zonal transport[2] $T_{\text{BT}} = \int_{-H}^{0}\int_{0}^{L_y} u(z)\,dy\,dz$. The baroclinic transport is a more appropriate metric to compare simulations with and without topographic ridges. In flat channels, the barotropic transport is only balanced by bottom friction and can be several orders of magnitude larger than the baroclinic transport. With a ridge, the topographic form drag strongly reduces the barotropic flow. The baroclinic flow, instead, is a measure of the slope of the interface between the two layers in QG and the isopycnals in the PE simulations. This slope is set by a balance between the wind stress and the geostrophic eddies. Thus, a comparison of the baroclinic transport across different simulations will allow us to characterize the role of topography on eddy properties.

Finally, it is worth pointing out that the Gaussian ridges considered in this work are sufficiently high to result in a very weak abyssal circumpolar flow. Thus, the baroclinic and barotropic transports are very similar in all simulations with topography for all but the weakest winds, that is, provided that the flow is baroclinically unstable and eddies transfer momentum downward to the bottom topography.

3. Dynamical framework

a. Reference QG numerical experiment

Our first set of experiments is designed to investigate the transition from channel-like to basinlike circulations

[1] This value is equivalent to the one used in the QG model since bottom drag is applied in the bottom level only, and the depths of the bottom level are 2800 and 210 m in the QG and PE simulations, respectively.

[2] Notice that with these definitions, the total transport is not equal to the sum of the barotropic and baroclinic transports.

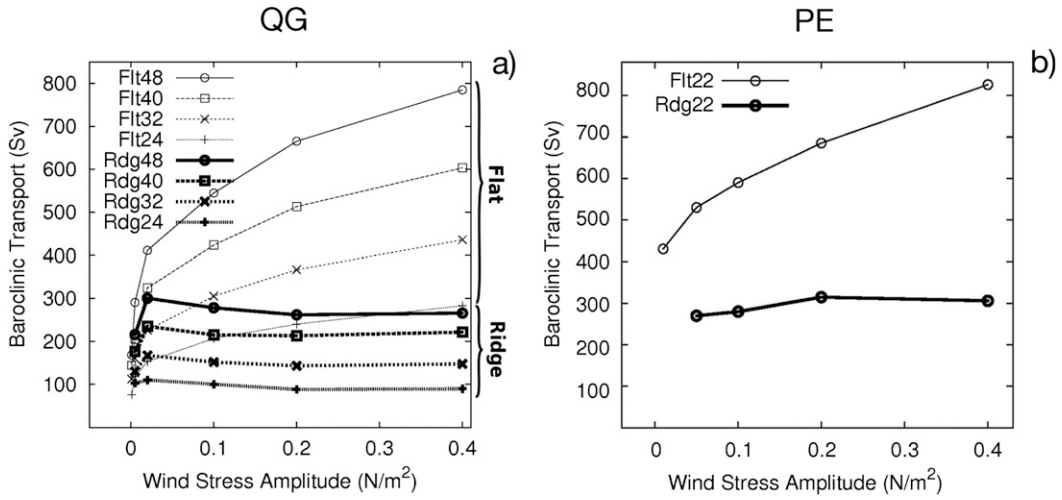

FIG. 2. Time average baroclinic transport sensitivity to wind stress amplitude for (a) the quasigeostrophic model and (b) the primitive equation model. Thin lines correspond to flat bottom experiments, and thick lines correspond to Gaussian ridge experiments. Each series of experiments are repeated using four different Rossby radii: $L_\rho = 24$, 32, 40, and 48 km. In the primitive equation experiments, only one Rossby radius was used: $L_\rho = 22$ km.

shown in the two panels of Fig. 1 for the Channel+Ridge case. More precisely, we want to understand why a gyre circulation develops in the lee of the topographic ridge and what role it plays in setting the transport along the channel. A useful starting point is to compare channel simulations with and without a Gaussian ridge topography.

Figure 2a shows the baroclinic transport diagnosed from quasigeostrophic simulations of a flat bottom channel and a channel with a ridge for a set of different wind stresses and Rossby radii (i.e., different reduced gravity g'). In the flat channel simulations, the baroclinic transport increases as $\tau^{0.2}$ for wind stresses ranging from $\tau_0 = 0.001$ to $0.4\,\mathrm{N\,m^{-2}}$. When a Gaussian ridge is introduced, the baroclinic transport becomes independent of the wind stress for winds stronger than $\tau_0 = 0.001\,\mathrm{N\,m^{-2}}$. In both cases, the baroclinic transport increases with the internal deformation radius as $L_\rho^{1.4}$.

The flat bottom results are consistent with the traditional view of the momentum budget in oceanic channels. The baroclinic transport is set through a balance between the transient eddy field and the wind forcing. As the wind is increased, the eddy field increases and partly offsets the increase in the overall transport as predicted by theories of downward transfer of zonal momentum by eddy form drag (e.g., Johnson and Bryden 1989; Marshall and Radko 2003) and observed in other flat bottom numerical studies (e.g., Tansley and Marshall 2001). Marshall and Radko (2003) argued that the baroclinic transport is proportional to the wind stress magnitude τ_0 and inversely proportional to the effective eddy diffusivity κ, a measure of the eddy intensity. Thus, we infer that in our flat channel simulations the eddy diffusivity increases as $\kappa \sim \tau^{0.8}$, so as to give $T_{\mathrm{BC}} \sim \tau_0/\kappa \sim \tau^{0.2}$.

When a ridge is added, the dynamics change in a fundamental way. The leading-order balance of zonal momentum is between the surface wind stress and the topographic form drag at the ridge. A large-scale standing wave pattern in the form of a recirculating gyre develops in the lee of the ridge. Olbers et al. (2004) argued that the leading-order balance between winds and transient eddies can be recovered if one takes averages along the mean flow streamlines. However, this approach does not explain what sets the gyre recirculation and why the transport is no more sensitive to the wind stress. In the following, we will argue that a gyre develops in the lee of the ridge, as long as the wind stress is not constant with latitude and thus has a curl. The bottom form drag associated with this gyre balances the surface wind stress. Any increase in winds spins a faster gyre, resulting in a larger bottom form drag, without any significant increase in the along-channel transport. In this view, the saturation of the transport is connected to the topographic form drag exerted by the gyre, which is absent in the flat bottom simulations.

b. *The gyre mode and the circumpolar mode*

The left panels of Fig. 3 show the barotropic streamfunction ψ_{BT} for different wind forcing in the Channel+Ridge simulations. The light gray shaded areas show closed barotropic streamlines, that is, recirculating gyres, whereas the blue shaded areas highlight circumpolar streamlines. The barotropic streamfunction becomes progressively more similar to that from the

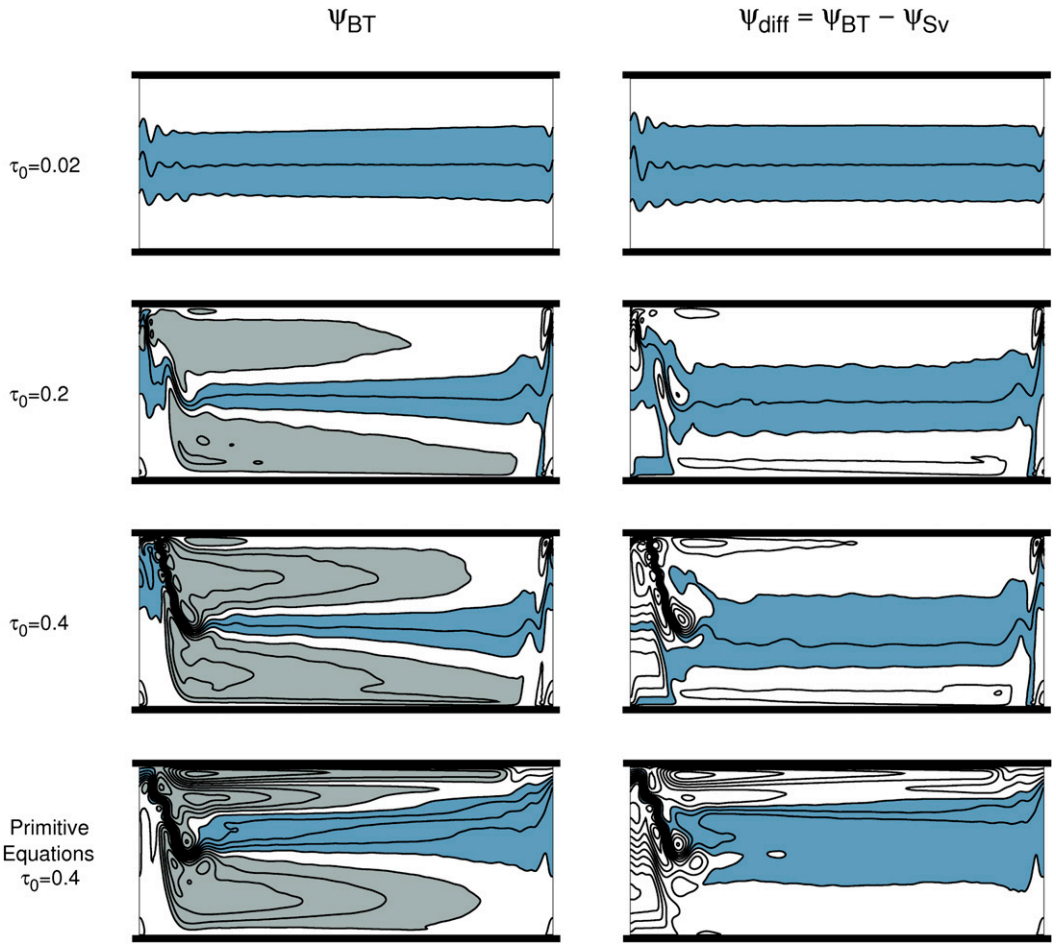

FIG. 3. (left) Time-mean barotropic streamfunction ψ_{BT} and (right) difference between the observed barotropic streamfunction and the analytic Sverdrup streamfunction ψ_{diff} for three different wind forcings: $\tau_0 = 0.02$, 0.2, and 0.4 N m^{-2}. The light gray shaded areas show closed barotropic streamlines, and the blue shaded areas show circumpolar streamlines. The Rossby radius of deformation is 24 km. Bottom row shows results obtained using the PE model for an experiment similar to QG at $\tau_0 = 0.4$ N m^{-1}.

Box+Ridge simulations for increasing wind stress. We thus propose to interpret the barotropic circulation in the Channel+Ridge simulations as the sum of a basin closed circulation and a channel circumpolar one.

The barotropic circulation in the Box+Ridge simulations is very well described by the Sverdrup solution in the ocean interior east of the western boundary current (Pedlosky 1996):

$$\psi_{SV}(x,y) = -\frac{1}{\rho_0 H\beta}\int_x^{L_x} \mathrm{curl}_z\boldsymbol{\tau}\, dx, \qquad (3)$$

where we set $\psi_{SV} = 0$ on the eastern boundary at $x = L_x$. We test our hypothesis by subtracting the Sverdrup solution in Eq. (3) from each of the Channel+Ridge streamfunctions ψ_{BT} in Fig. 3 and checking if the residuals ψ_{diff} are circumpolar streamfunctions. The ψ_{diff} is composed of three reentrant streamlines, and it is indeed a circumpolar circulation with strength largely independent of the wind stress amplitude. This supports our hypothesis that the total barotropic streamfunction can be decomposed in a ''gyre mode'' (Sverdrup gyres), contributing no vertically integrated circumpolar transport, and a purely zonal ''circumpolar mode,'' contributing all the barotropic transport. This decomposition does not constitute a formal mathematical basis, and the term ''mode'' is used somewhat loosely to identify the two components of the circulation.

As winds are increased, the baroclinic circumpolar transport (which equals the barotropic transport in this case) does not increase because the wind forcing goes into strengthening the gyre circulation. In other words, the additional forcing strengthens the gyres but does not affect the circumpolar mode.

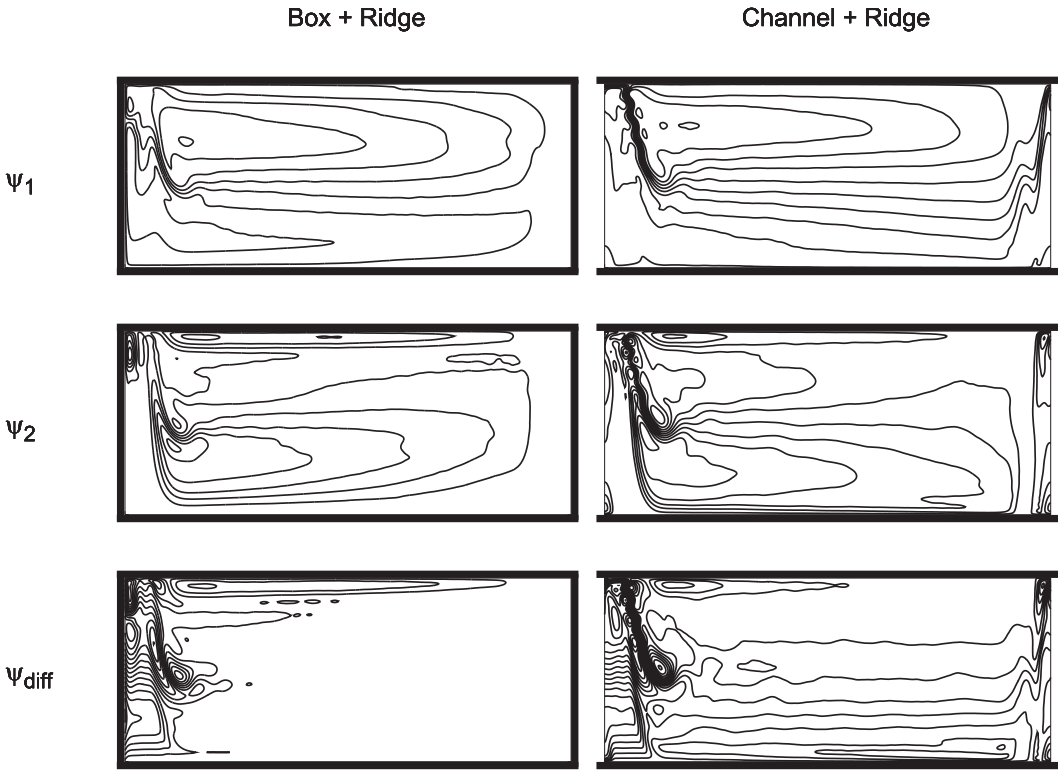

FIG. 4. Time-mean (top) upper- and (middle) lower-layer streamfunction ψ_1 and ψ_2 and (bottom) difference between the observed barotropic streamfunction and the analytic Sverdrup streamfunction ψ_{diff} for the (left) Box+Ridge and (right) Channel+Ridge geometries. The wind stress amplitude is $\tau_0 = 0.4\,\text{N}\,\text{m}^{-1}$, and the Rossby radius of deformation is 24 km.

c. *Comparison with primitive equation numerical results*

Figure 2b shows the baroclinic transport diagnosed from Channel+Flat and Channel+Ridge simulations performed with the PE model for a Rossby radius[3] $L_\rho =$ 22 km. Although the values of baroclinic transport do not match exactly those obtained with the QG model, the qualitative dependence on the wind stress agree nicely. The bottom panels of Fig. 3 show barotropic streamfunction and ψ_{diff} from the PE simulations initialized with $L_\rho = 22$ km and forced with the same wind stress $\tau_0 = 0.4\,\text{N}\,\text{m}^{-1}$ as the QG simulation used for the panel right above. The PE and QG barotropic flows are very similar in the interior, away from the boundaries, where the gyre circulation is prevalent. The close agreement between the simple two-layer QG model and the more complex 25-level PE model builds our confidence that QG dynamics can be used to interpret more realistic channel models.

d. *Dynamics of the gyre mode*

Our discussion of the gyre mode should not be taken to imply that the development of the recirculating gyre in the Channel+Ridge simulations can be understood in terms of Sverdrup linear vorticity dynamics. The crucial role played by eddies in setting up the channel circulation is illustrated in Fig. 4, where we plot separately the upper- and lower-layer streamfunctions ψ_1 and ψ_2 for both the Box+Ridge and the Channel+Ridge simulations. The bottom row of the figure shows the difference between the observed barotropic streamfunction and the analytic Sverdrup streamfunction ψ_{diff}. Consistent with what we showed above, in the Box+Ridge basin simulations ψ_{diff} is zero away from the boundaries, and the barotropic flow is approximately in Sverdrup balance. However, there is interesting vertical structure to the double-gyre circulation. The northern gyre is confined to the upper layer, while the southern gyre resides in the lower layer (first and second left panels in Fig. 4). The circulation observed in the lower layer must be

[3] The Rossby radius varies spatially from 10 km in the south of the channel to almost 40 km in the north of the channel. The value of 22 km given in Fig. 2 comes from a spatial average of the Rossby radius across the domain.

driven by vortex stretching associated with transient eddies, including transient zonal jets, because winds act only on the upper layer (NS09). To stress the crucial role of transient eddies, we refer to this circulation as basinlike gyres in contrast to the linear barotropic basin gyres in Sverdrup balance.

Similarly to the Box+Ridge simulations, the northern gyre is mostly confined to the upper layer, and the southern gyre is mostly confined to the lower layer in the Channel+Ridge simulations. In the lower layer, the southern gyre is approximately 2.5 times stronger than the northern gyre. The circumpolar mode is instead confined to the upper layer. In the next few sections, we will test the hypothesis that the spinup of the bottom-layer circulation by eddies sustains the topographic form drag that balances the surface wind stress and causes the saturation of the circumpolar transport.

In this section, it remains to be explained why the barotropic transport is so similar in the Box+Ridge and Channel+Ridge simulations, despite the fact that there are lateral walls in the former but not in the latter. Using the planetary geostrophic equations, Salmon (1992) showed that a western boundary current can detach from the western wall and follow f/h contours when continental shelf topography is added to Stommel's solution (Stommel 1948). If the topography is sufficiently steep to bring geostrophic contours close together, a frictional boundary layer develops that acts as an "effective wall." In other words, the flow follows f/h until the contours are so close together that lateral mixing diffuses PV and allows the flow to turn around and close the gyre circulation (Salmon 1992). Alternatively, one can interpret the steering of the flow as the result of the force generated by a topographic form drag. In a turbulent stratified ocean, eddy vortex stretching transfers momentum downward and barotropizes the flow. In the Box+Ridge solution shown in Fig. 4, this occurs mainly over topography and the jet exit region, where the eddy activity is strongest (not shown) and the circulation has a prominent barotropic component. In turn, this barotropization allows the wind-driven upper layer to feel the topography through topographic form stress. The role of the actual western wall in closing the vorticity budget in such a basin circulation is secondary. A posteriori, it is therefore not too surprising that the basinlike circulation survives the removal of meridional boundaries in the Channel+Ridge simulations.

1) VORTICITY BALANCE

The claim that Salmon's interpretation of wind-driven flows over uneven topography applies to our simulations can be formally tested by verifying that the barotropic vorticity budget for the open and closed basins are very similar. The vertically averaged vorticity budget can be written as

$$\beta\frac{\partial\overline{\psi_{\mathrm{BT}}}}{\partial x}+\frac{H_1}{H}\overline{\mathrm{J}(\psi_1,\nabla^2\psi_1)}+\frac{H_2}{H}\overline{\mathrm{J}(\psi_2,\nabla^2\psi_2)}+\mathrm{J}\left(\overline{\psi_2},\frac{f_0}{H}h_b\right)=\frac{\hat{\mathbf{k}}\cdot\nabla\times\boldsymbol{\tau}}{\rho_1 H}-r\frac{H_2}{H}\nabla^2\overline{\psi_2},\tag{4}$$

where $\psi_{\mathrm{BT}}=\psi_1+\psi_2$ and the overbars denote the 200-yr temporal average; J[] is the Jacobian operator; r is the bottom drag coefficient; and $\mathbf{k}$ is a unit vector in the vertical direction. Figure 5 shows the different terms in Eq. (4) integrated latitudinally over the southern gyre as a function of longitude for the Box+Ridge and Channel+Ridge simulations. The southern gyre corresponds to the southern half of the domain except in the western boundary region, where it extends northward following the contour of $\psi_{\mathrm{BT}}=0$. (Similar results are obtained for the northern gyre.) The first three terms on the left-hand side of Eq. (4) are summed up and labeled β+NL.

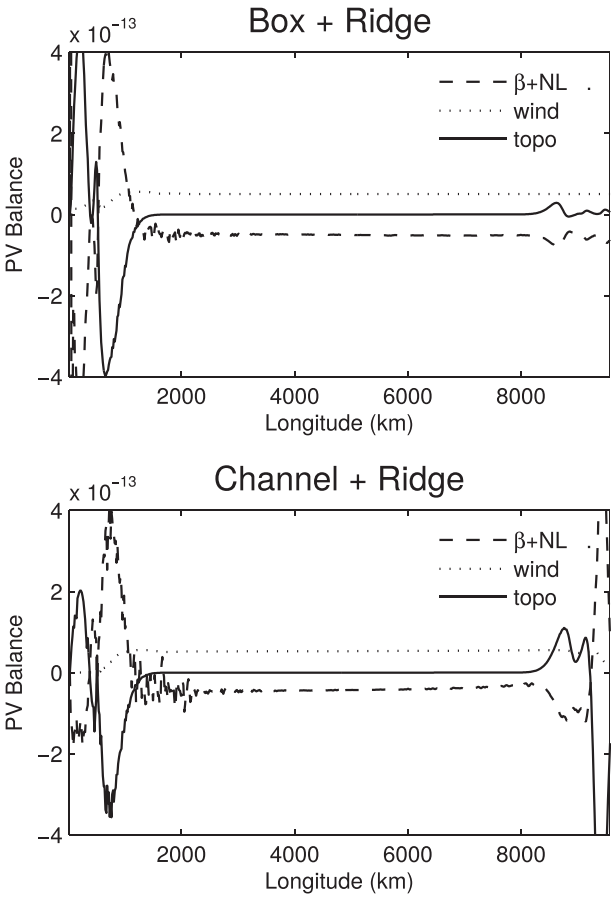

FIG. 5. Main terms in the barotropic potential vorticity Eq. (4) for (top) the Box+Ridge and (bottom) the Channel+Ridge simulations shown in Fig. 4.

The fourth term on the left-hand side, representing the topographic form stress, is labeled "topo." The first term on the right-hand side is labeled "wind." Friction, the last term on the right-hand side, is negligible in comparison to the other terms at every latitude. The budgets are very similar in the Box+Ridge and the Channel+Ridge simulations. In the interior, away from boundaries and topography, there is a balance between the β+NL term (dominated by β) and the wind—this is the Sverdrup balance. Over the ridge, the topographic term is balanced by both the β and NL terms. The two simulations differ only in a small region close to the lateral boundaries where the presence of the meridional walls enhances somewhat the topographic form drag. The close similarity between the Box+Ridge and Channel+Ridge vorticity budgets confirms our inference that the dynamics are similar in the two cases and largely independent of the presence of the meridional walls. While the gyre circulations are very similar in the Box+Ridge and Channel+Ridge simulations, the latter allows for an additional circumpolar transport not possible in the former.

2) EDDY MOMENTUM TRANSFER

We now focus on how the addition of a ridge affects the vertical transfer of zonal momentum in the channel. Recall that with topography bottom friction is not a significant sink of zonal momentum. Neglecting dissipations terms, the dominant zonal momentum balance at statistical equilibrium in each layer can be written as

$$\langle \psi_{1x}\psi_{1yy}\rangle - \frac{f_0^2}{g'H_1}\langle \psi_2\psi_{1x}\rangle - \frac{1}{\rho_0 H_1}\langle \tau\rangle = 0, \quad \text{and} \quad (5)$$

$$\langle \psi_{2x}\psi_{2yy}\rangle - \frac{f_0^2}{g'H_2}\langle \psi_1\psi_{2x}\rangle + \frac{f_0}{H_2}\langle \psi_{2x}h_b\rangle = 0, \quad (6)$$

where brackets $\langle\ \rangle$ represent zonal and temporal averages. The first two terms in each equation are the Reynolds stress and interfacial form stress. The last terms represent momentum input by the wind in the upper layer and its removal by topographic form drag in the bottom layer. A calculation of the terms in Eqs. (5) and (6) confirms that the momentum is input by the wind at the surface, transported downward by geostrophic eddies via interfacial form stress, and lost through topographic form drag at the ocean bottom. In our experiments, the Reynolds stress terms are small compared to the wind stress and the interfacial form drag. A spectral decomposition of the interfacial form stress term illustrates which scales are most efficient at transferring momentum downward. In Fig. 6, we show the contribution of different zonal wavenumbers to the zonally averaged form stress in channel simulations with and without topography. At every time step, we perform a Fourier transform of the streamfunction in each layer in the zonal direction: $\psi_n = \sum_k A_n(k, y, t)\cos(kx) + B_n(k, y, t)\sin(kx)$. The contribution of wavenumber k to the zonal form stress is then given by a time and meridional average of $T(k, y, t) = (k/2)[A_1(k, y, t)B_2(k, y, t) - B_1(k, y, t)\, A_2(k, y, t)]$. We plot the time and meridional average of $kT(k, y, t)$ as a function of $\ln(k)$ so that the area under the curve is proportional to the stress at that scale.

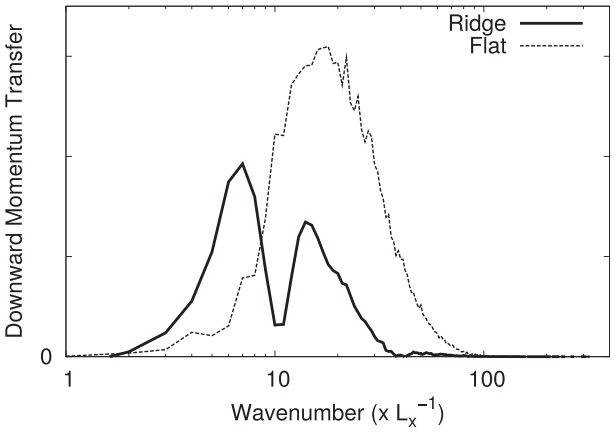

FIG. 6. Spectral decomposition according to zonal wavenumber k of the interfacial form stress term in a flat bottom channel (labeled Flat) and in a channel with a Gaussian ridge (labeled Ridge).

Figure 6 shows that the momentum transfer is fundamentally altered by the addition of a ridge. With a flat bottom, the time-mean flow is purely zonal. At every latitude, momentum transfer is accomplished by transient mesoscale eddies, with characteristic wavenumber 20. In contrast, with a Gaussian ridge the time-mean flow is zonally asymmetric, and the momentum transfer is dominated by a much larger wavenumber ($k \simeq 6$). Notice that the bimodality in the spectrum is the consequence of an inertial recirculation developing directly over the topographic ridge; this creates a strong peak at the ridge wavelength. NS12 also reported the same result. With a Gaussian ridge, the momentum transfer is dominated by larger-scale standing eddies (see also Thompson and Naveira Garabato 2014; Abernathey and Cessi 2014). These results support the hypothesis that the gyres—large-scale standing structures—dominate the momentum balance in the channel.

4. Testing the framework

a. *Effect of the ridge height*

Salmon (1992) pointed out that, in a closed basin with a continental shelf topography, neither friction nor inertia play a leading-order role in setting the circulation

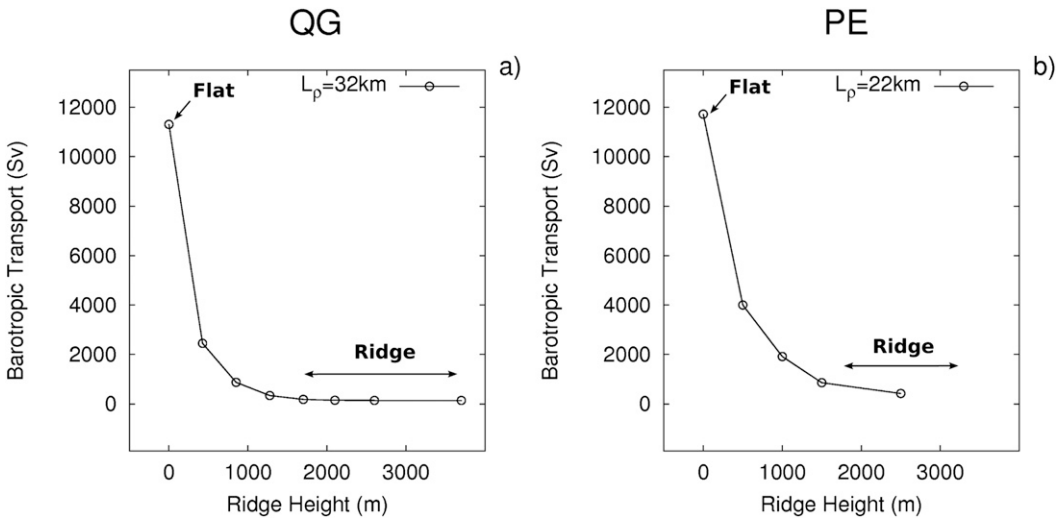

FIG. 7. Time-mean barotropic transport sensitivity to ridge height for (a) the QG model and (b) the PE model. The Rossby radius of deformation is 32 km in QG and 22 km in PE, and the wind stress amplitude $\tau_0 = 0.4\,\mathrm{N\,m^{-2}}$.

pattern along most of the western boundary. The flow simply follows the barotropic geostrophic contours, $\beta_y + (f_0/H)h_b$ [see Eq. (4)], until they come close enough for friction to take over and allow the contours to close. In a channel geometry, it is interesting to ask how high the topography needs to be in order to observe basinlike dynamics. Figure 7 shows results from a series of QG and PE model experiments all forced with $\tau_0 = 0.4\,\mathrm{N\,m^{-2}}$ but configured with Gaussian topographic bumps of different heights h_0. The transport drops quickly as h_0 is increased from 0 to 1000 m and reaches an equilibrium value for $h_0 > 2000$ m. This equilibrium regime defines what we refer to as the "ridge case" throughout this work, achieved when topography blocks the last open barotropic geostrophic contour.

Figure 8 shows the barotropic streamfunction and geostrophic contours $\beta_y + (f_0/H)h_b$ for increasing topographic height h_0 from the QG simulations. Circumpolar streamlines (blue shaded areas) follow the geostrophic contours for every value of h_0. The number of circumpolar streamlines, however, decreases rapidly with h_0. The barotropic transport drops from 2450 Sv for $h_0 = 425$ m to 143 Sv for $h_0 = 2600$ m. As the transport drops, the geostrophic contours close and a recirculating gyre develops. An asymptotic regime is reached in transport when the last geostrophic contour is closed at $h_0 = 1770$ m. This also coincides with the limit where the bottom-layer circumpolar transport tends to zero (not shown).

b. *Effect of the channel length*

According to our hypothesis, the strength of the recirculating gyre is given by Sverdrup's relationship Eq. (3) and must increase with the channel length L_x. Furthermore, we implicitly assumed that the recirculating gyres always span the whole channel. The circumpolar circulation instead should not depend on L_x. Figure 9 shows the barotropic streamfunction and barotropic zonal transport from a suite of experiments configured with different channel lengths (L_x = 3000, 6000, 10 000, and 19 000 km). Consistent with the above framework, the basinlike gyres become more and more prominent as the channel gets longer. Regardless of the channel length, the gyres always span the whole domain, which suggests that the effect of topography is best thought of as a global constraint instead of a standing Rossby wave or storm track confined in the lee of the ridge.

The right-hand side panel of Fig. 9 shows transport as a function of L_x for two different stratifications. The zonal transport does not change with increasing channel length, supporting the hypothesis that the flow can be decomposed in a gyre mode that has no circumpolar contribution and a circumpolar mode and that carries all zonal transport. Varying L_x modulates the strength of the gyre mode but leaves the circumpolar mode unaltered. This suggests that planetary-scale gyres may be present in the ACC in the lee of major topographic barriers, but they may be difficult to diagnose because of the irregular topography.

c. *Effect of wind stress curl*

According to flat channel theories (e.g., Johnson and Bryden 1989; Marshall and Radko 2003), the ACC transport is set by the wind stress applied over the channel and is independent of the wind stress curl. Our

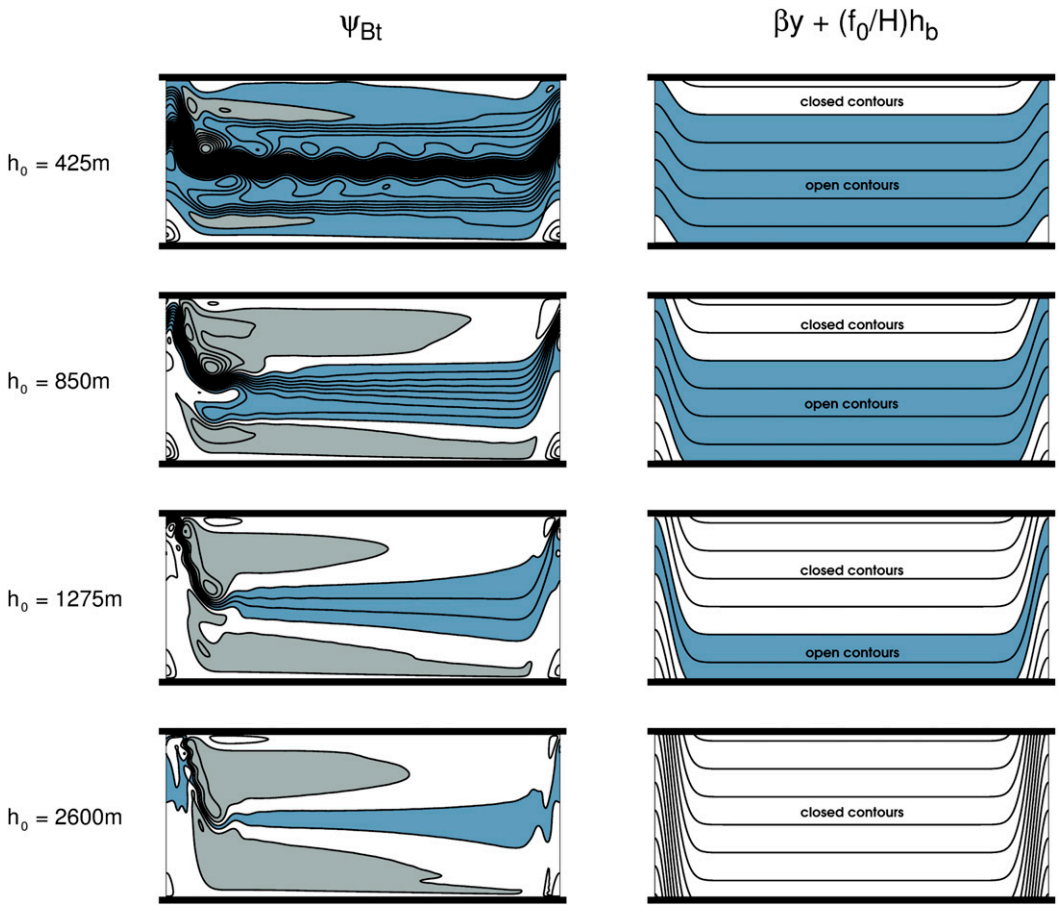

FIG. 8. (left) Time-mean barotropic streamfunction ψ_{BT} and (right) geostrophic contours $\beta_y + (f_0/H)h_b$ for different ridge heights. (left) The light gray shaded areas show closed barotropic streamlines, and the blue shaded areas show circumpolar streamlines. (right) Blue shaded areas highlight open contours. The Rossby radius of deformation is 32 km.

hypothesis instead suggests that, for a given wind stress, the zonal transport may increase for a reduction in wind stress curl because the gyre circulation and its associated bottom form drag get weaker. The sensitivity of the channel transport to the wind stress curl has already been reported by NS12, who considered the circulation in a channel connected to a closed basin to the north. Here, we extend the study to a channel-only configuration. We consider simulations forced with a wind stress of the form

$$\boldsymbol{\tau} = \frac{1}{2}\tau_0[1 - \tau_{\text{curl}}\cos(2\pi y/L_y)]\mathbf{I}, \tag{7}$$

where τ_0 sets the wind stress amplitude (N m^{-2}), and τ_{curl} is the fraction of the wind stress that contributes a curl. By construction, the value of τ_{curl} does not affect the globally averaged wind stress input in the channel. When $\tau_{\text{curl}} = 1$, the latitudinal stress profile corresponds to the $\sin^2(\pi y/L_y)$ reference wind. When $\tau_{\text{curl}} = 0$, a constant wind stress is applied everywhere in the channel.

Figure 10 shows how the baroclinic along-channel transport varies for increasing wind stress magnitude τ_0 for three values of $\tau_{\text{curl}} = 1$, 1/2, and 0 using the Channel+Ridge configuration. For comparison, we also show the results for the Channel+Flat configuration using $\tau_{\text{curl}} = 1$; the value of τ_{curl} does not alter significantly the results for this case. The overall scalings are similar for different L_ρ, that is, stratification.

The baroclinic transport increases for decreasing wind stress curl in all Channel+Ridge simulations (Fig. 10). The wind stress curl accounts for approximately half of the difference between Channel+Ridge and Channel+Flat cases using the reference wind. Figure 11 shows how the circulation changes as the wind stress curl goes to zero. The barotropic streamfunction ψ_{BT} becomes zonally symmetric in the interior as the curl vanishes (left panels of Fig. 11) and the bottom-layer recirculating gyres disappear (right panels in Fig. 11).

The bottom panels of Fig. 11 show an experiment using a wind stress with $\tau_{\text{curl}} = 0$ and the PE model. The

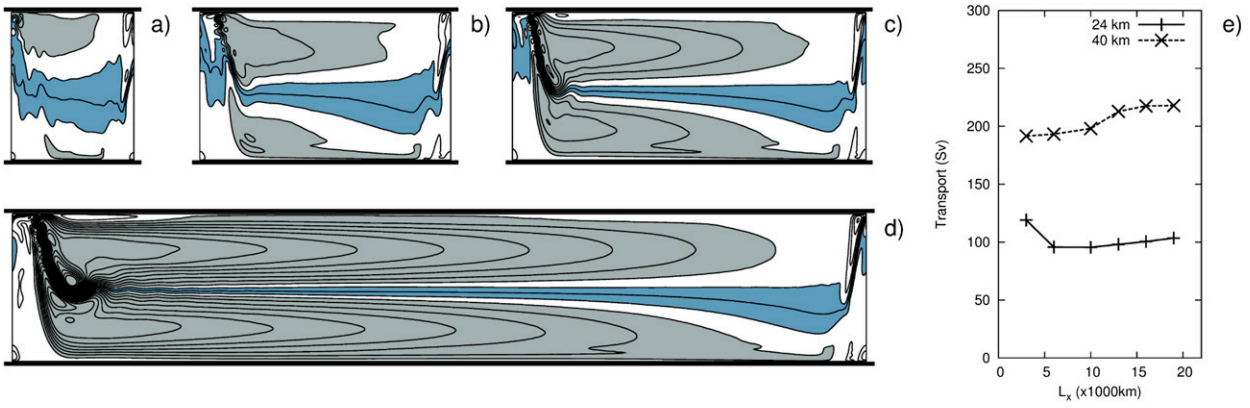

FIG. 9. Sensitivity to the channel length. Barotropic streamfunction for (a) $L_x = 3000$ km, (b) $L_x = 6000$ km, (c) $L_x = 10\,000$ km, and (d) $L_x = 19\,000$ km. (e) Transport sensitivity to L_x for two different Rossby radii $L_\rho = 24$ and 40 km. In the left panels, the Rossby radius is 24 km.

PE solution is very similar to the QG one. In both cases, the flow is zonally symmetric in the interior away from the Gaussian bump. Strong boundary currents are observed at the northern and southern walls due to Ekman flux convergence and divergence. Without any wind stress curl, the transport in the PE model increases from 230 Sv for $\tau_{\text{curl}} = 1$ (Fig. 3) to 370 Sv for $\tau_{\text{curl}} = 0$ (Fig. 11).

Figure 10 suggests that the saturation of the transport observed using the reference wind in the Channel+Ridge simulations may be partly the result of increasing both wind stress and wind stress curl at the same rate. Simulations with $\tau_{\text{curl}} = 0$ show that the baroclinic transport increases somewhat for increasing τ_0 but still much less than in Channel+Flat simulations.

The presence of a wind stress curl has very different impacts on channels with and without topography. In the flat bottom case, the input of zonal momentum by the wind is balanced by the bottom friction $\langle \tau \rangle = \langle r u_2 \rangle$, which sets the bottom-layer average zonal velocity and varies linearly with the wind stress, independent of the curl. When a ridge is added, the input by the wind is balanced by topographic form drag $\langle \tau \rangle = \langle v_2 h_b \rangle$. When $\tau_{\text{curl}} = 1$, this drag is achieved by the western boundary current that closes the Sverdrup gyres and flows along the ridge; the boundary current increases linearly with the wind stress curl. When $\tau_{\text{curl}} = 0$ and gyres are absent, the topographic drag is associated with a standing meander developing on the ridge.

Notice that for the Channel+Ridge simulation, the form stress on the ridge is the main sink of zonal momentum even when $\tau_{\text{curl}} = 0$. We performed a spectral decomposition of the form stress for this constant wind experiment (not shown). In this case, the momentum transfer is shifted toward higher wavenumbers compared to the reference $\tau_{\text{curl}} = 1$ case. This shift was also observed by NS12 in a similar set of experiments varying the wind stress curl. They hypothesized that transient eddies transfer zonal momentum downward in the absence of basin gyres.

d. *Effect of bottom friction*

In a QG setup similar to the one used in this manuscript, Hogg and Blundell (2006) observed that the circumpolar transport increases with increasing bottom friction. They suggested that this is a result of eddy saturation; increasing friction decreases the strength of

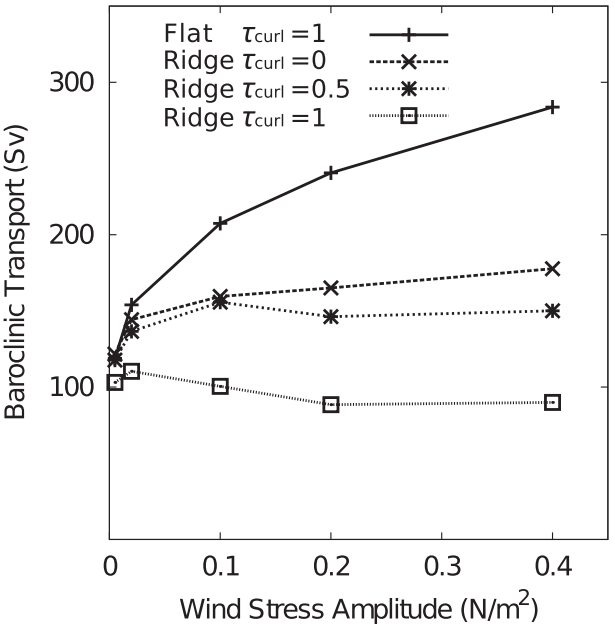

FIG. 10. Time average baroclinic transport sensitivity to the relative amount of wind stress curl τ_{curl} [see Eq. (7)]. Results for a flat bottom channel with the reference wind are also shown.

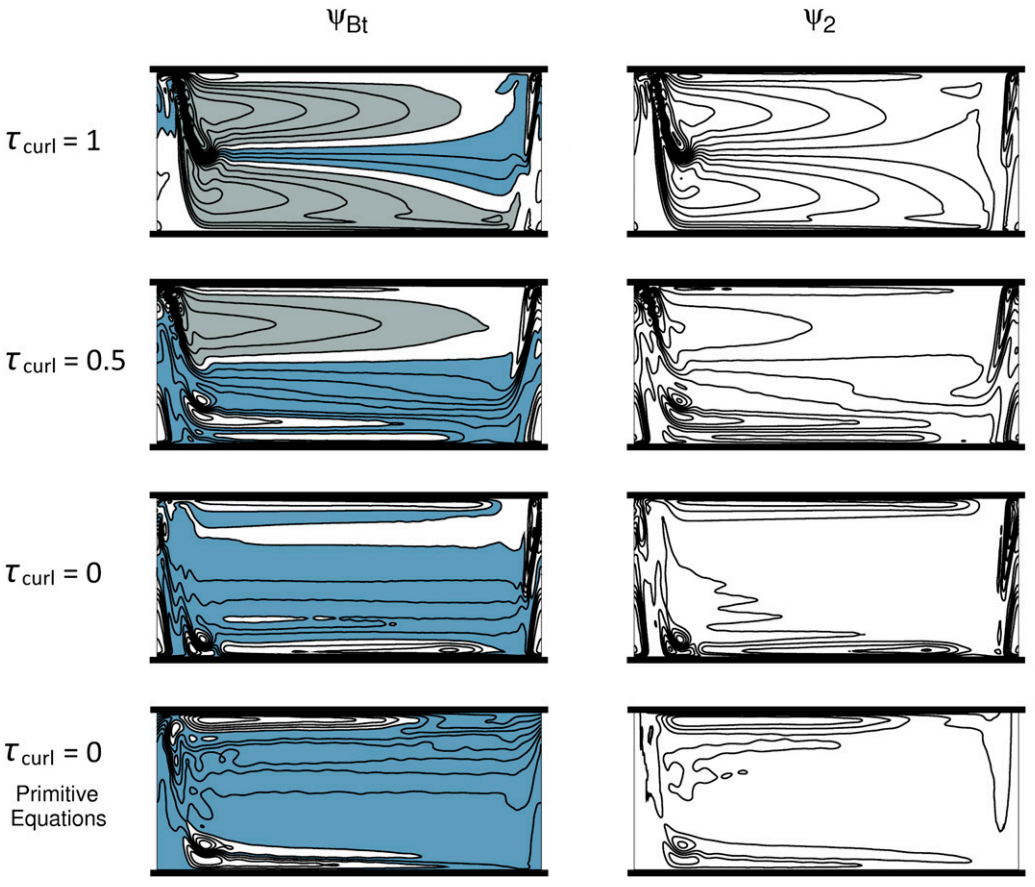

FIG. 11. (left) Time-mean barotropic streamfunction ψ_{BT} and (right) bottom-layer streamfunction ψ_2 for three different wind stress curl: $\tau_{curl} = 1$, 0.5, and 0. As before the light gray shaded areas show closed barotropic streamlines, and the blue shaded areas show circumpolar streamlines. The Rossby radius of deformation is 24 km. Bottom row shows results obtained using the PE model for an experiment similar to QG at $\tau_{curl} = 0$.

transient eddies, which reduces the downward transport of momentum and increases the transport. NS12 also observed increasing circumpolar transport with increasing bottom friction in a channel connected to a closed basin to the north. They suggested that increasing friction weakens the recirculating gyre in the channel and more of the southward Sverdrup transport from the basin contributes to the circumpolar flow. We now revisit these results using our channel setup.

Figure 12 shows baroclinic and barotropic transport results for different wind forcings for the Channel+Flat and Channel+Ridge simulations. In the flat bottom channel, with weak friction, the barotropic transport largely exceeds the baroclinic transport because the bottom velocities must be large to balance the wind forcing. As friction increases and bottom velocities become smaller, the barotropic transport drops until it equals the baroclinic one at strong friction. In the ridge case, the baroclinic transport always equals the barotropic transport since topography blocks the bottom circumpolar flow. Similarly to what was observed by Hogg and Blundell (2006) and NS12, the transport increases with bottom friction when topography is added. Notice that the transport is independent on the wind stress only for bottom drag coefficients smaller than $r < 5 \times 10^{-7} s^{-1}$. For very large drag coefficients, the flat bottom and ridge solutions converge because the bottom velocities become small in both setups. Note that stratification does not alter the general behavior of the transport (not shown).

Figure 13 shows the top- and bottom-layer streamfunctions for different values of drag coefficients corresponding to Fig. 12. As drag increases, the strength of the bottom-layer recirculating gyres gets weaker. Simultaneously, the upper-layer streamfunction becomes more zonally symmetric. This suggests that the primary effect of bottom friction is to inhibit the development of the gyre mode, leaving only the free circumpolar mode at high values of friction (bottom panels in Fig. 13). From a momentum balance

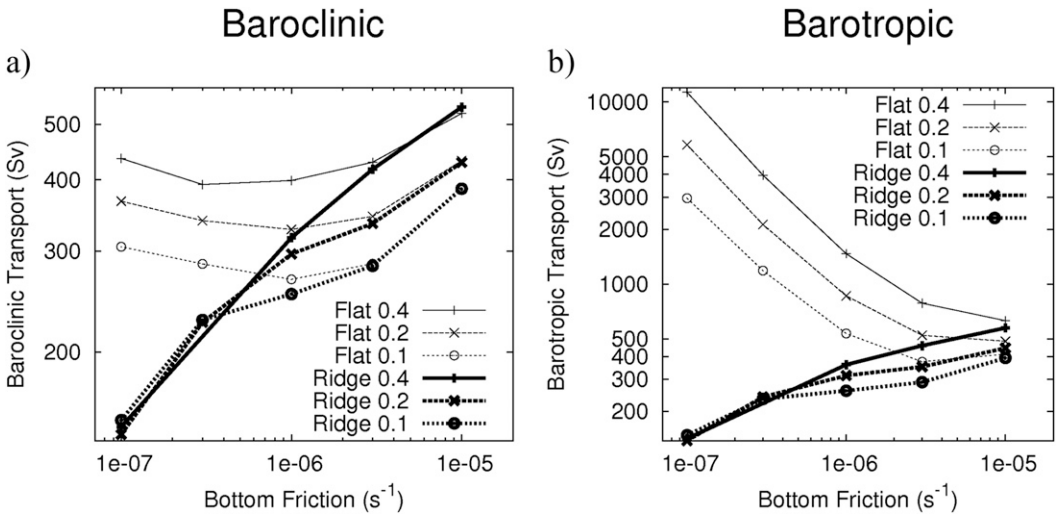

FIG. 12. Time-mean (a) baroclinic and (b) barotropic transport sensitivity to bottom friction for the flat bottom and Gaussian ridge at three different wind forcing amplitudes: $\tau_0 = 0.1$, 0.2, and 0.4 N m^{-2} (labeled Ridge 0.1, 0.2, and 0.4, respectively). The Rossby radius of deformation is 32 km.

perspective, the large drag coefficients damp the gyre mode and its associated topographic form drag. The circumpolar mode must therefore increase to provide the necessary drag.

Experiments varying friction using the primitive equation model have also been performed. These show a behavior similar to that observed using the QG model. For example, transport increases from 230 to 350 Sv for a tenfold increase in the bottom drag coefficient for the solution shown in the bottom panels of Fig. 3. Associated with this transport increase, the basinlike gyre is reduced by an amount similar to that shown for the QG simulation in Fig. 13.

One may naively expect that the experiments with high bottom friction presented here are equivalent to experiments with complex topography, but NSH13 show that this inference is misguided. Bottom friction suppresses the abyssal layer KE since energy dissipation is primarily via bottom drag. This results in the disappearance of the large-scale meanders in the lee of the ridge and much more zonally symmetric flow that does not saturate for strong winds. Complex topography, instead, redistributes the abyssal energy inside the domain and adds a number of large-scale meanders but nevertheless results in a saturation of the transport (see NSH13). Most recent modeling studies of the ACC show that (i) the circumpolar current has a number of major large-scale meanders (e.g., Mazloff et al. 2010) and (ii) its transport is saturated (e.g., Hallberg and Gnanadesikan 2006; Meredith et al. 2012). This suggests that the actual ACC behaves differently from the case of strong bottom friction explored here.

5. Discussion

We now apply the framework developed in this manuscript to interpret the circulation in the more realistic case of a channel connected to a basin to the north. In a series of three papers, NS09, NS12, and NSH14 studied the appearance of gyrelike circulations in a channel connected to a basin. In those papers, the gyrelike circulations developed as extensions of Sverdrup gyres present in basins north of the channel. Here, we suggest that the presence of a ridge in the channel acts as an effective wall that promotes the development of recirculating gyres, similar to that observed in a closed basin.

The hypothesis of NS09, sketched in the upper and middle panels of Fig. 14, was that the total transport is best thought of as the sum of a basin and a channel contribution. The channel contribution was argued to be constant and to correspond to the minimum shear for baroclinic instability, assuming no bottom flow. The basin contribution was instead the integrated meridional Sverdrup transport into the channel region. The transport was shown to increase with wind stress for weak winds (referred to as the Stommel regime), but to saturate for stronger winds (referred to as saturation regime). This saturation coincides with the development of a recirculating gyre in the channel. A fraction of the integrated meridional Sverdrup transport recirculated in a gyre rather than contributing to the circumpolar transport.

The channel-only simulations described in this paper suggest a different interpretation. The channel flow is best thought of as a superposition of a circumpolar mode (capturing all transport) and a gyre mode (recirculating

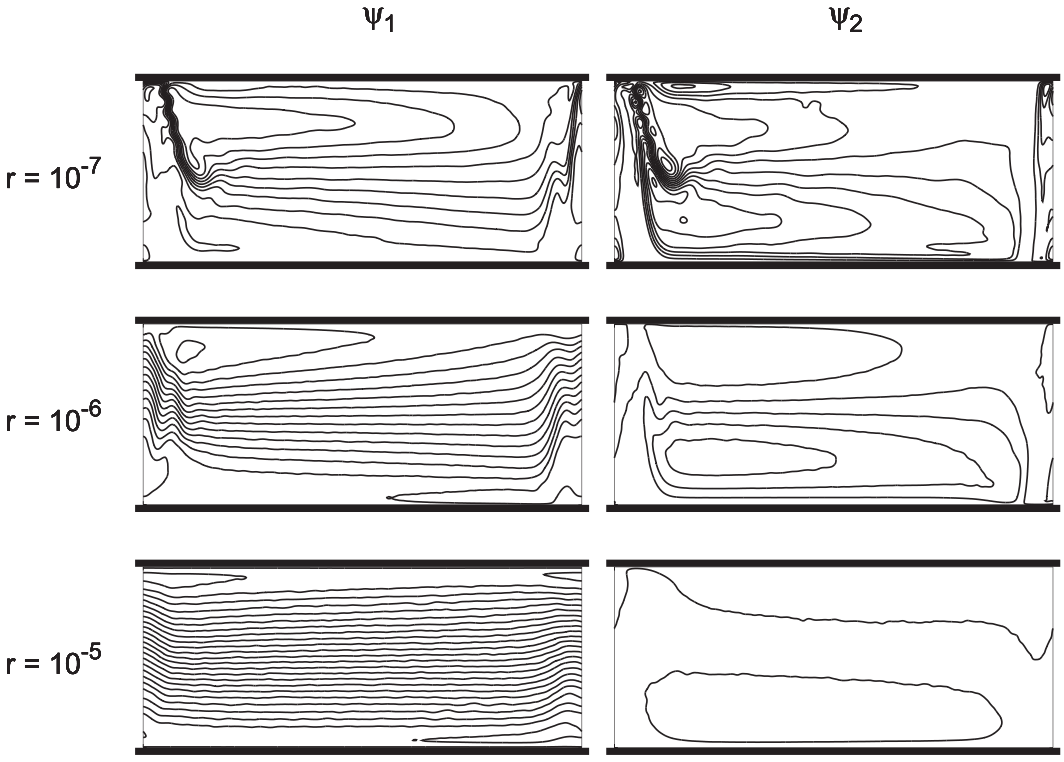

FIG. 13. Time-mean streamfunction in the (left) top and (right) bottom layers for three different values of bottom friction: $r = 10^{-7}$, 10^{-6}, and 10^{-5} s^{-1}.

gyres). In this view, the saturation of the circumpolar transport arises because the gyres strengthen with increasing wind so as to balance the surface input of momentum through topographic form drag.

An immediate advantage of the new hypothesis is that it removes the somewhat artificial separation between contributions emanating from the basin and the channel. For example, it is unclear how to define a channel contribution in the saturation regime using the NS09 hypothesis (panel marked with a question mark in Fig. 14). Yet, it is natural to interpret this saturation regime as the sum of a basin and circumpolar mode (lower panels of Fig. 3). Moreover, the vertical transfer of zonal momentum in the gyre provides a clear physical mechanism to explain transport saturation.

6. Conclusions

We considered the effect of a meridional ridge wider than the deformation radius on the dynamics of a wind-forced oceanic channel. In a flat bottom channel, the input of zonal momentum by the wind is balanced by bottom friction, and this establishes a link between forcing and zonal transport. We find that the baroclinic transport increases with the Rossby radius as $L_\rho^{1.4}$ and with the wind as $\tau_0^{0.2}$. This is consistent with the traditional view that the baroclinic transport is partially compensated by the strengthening of the eddy field for increasing wind stress. When a ridge is added, the wind input of momentum is balanced by topographic form drag and the baroclinic transport becomes insensitive to increasing wind forcing. Furthermore, closed recirculating gyres develop in the lee of the ridge. We suggested that the circulation is best described as the sum of a gyre mode (without any circumpolar contribution) and a circumpolar mode (contributing all the zonal transport). Any increase in winds results in a stronger gyre mode but does not affect the circumpolar mode. The gyre circulation provides the topographic form drag to balance the wind forcing, regardless of the strength of the circumpolar circulation. The strength of the gyre circulation increases linearly with the channel length and the wind stress curl, while it decreases with increasing bottom drag. The strength of circumpolar circulation is insensitive to the channel length; it increases with decreasing wind stress curl and increasing bottom drag.

Our framework is very different from that of Stommel (1957), who also emphasized the importance of gyre circulations to explain the ACC dynamics. Stommel invoked ad hoc lateral boundaries to support a large gyre, despite the fact that in the real ACC no such

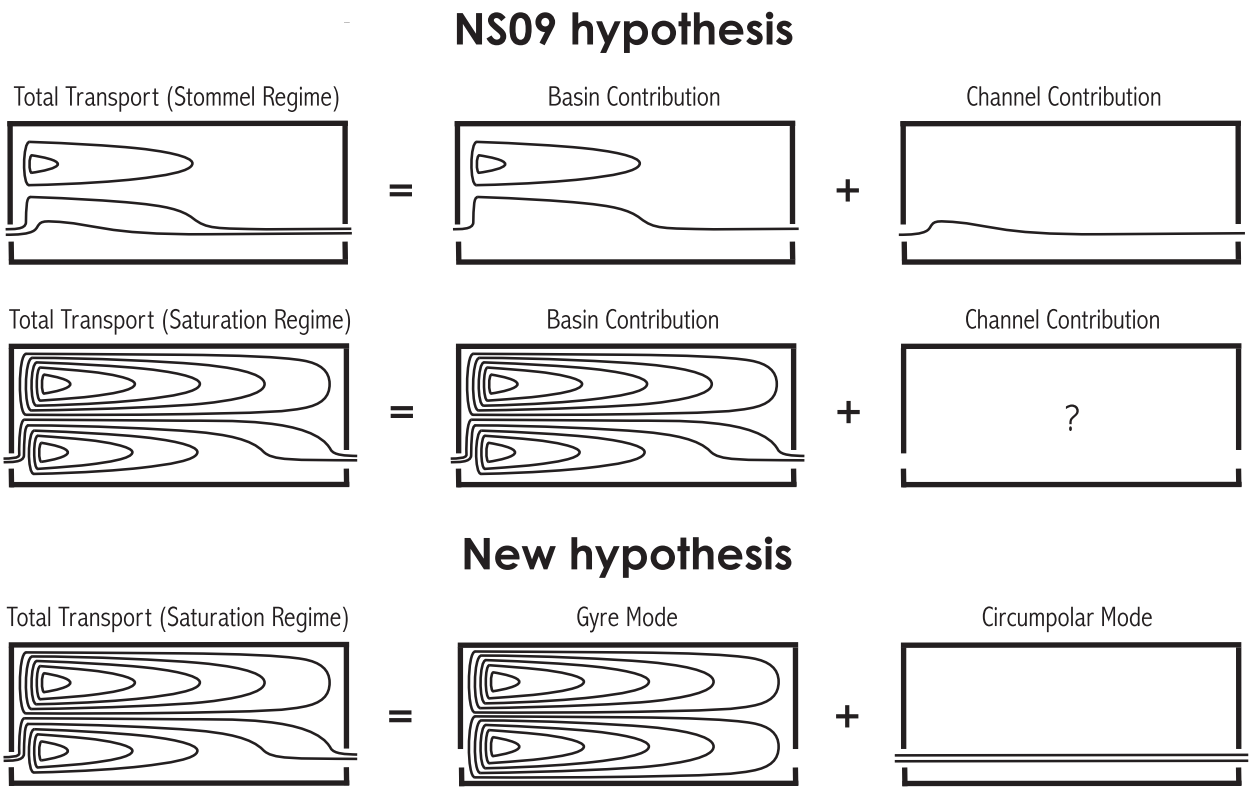

FIG. 14. Sketch of the barotropic streamfunction for the hypothesis of NS09 and the new hypothesis. In the hypothesis of NS09, the total transport is decomposed in a basin and a channel contribution, defined by the geographic division between the Drake Passage latitudes and the basin region to the north. In the revised hypothesis, all the circumpolar transport is expressed in the circumpolar mode. The gyre mode is intrinsically linked with the bottom form stress exerted by the ridge and affects the momentum balance in the channel such that the circumpolar mode is insensitive to the wind stress amplitude.

lateral continents exist in the latitude band of Drake Passage. We have shown that a barotropic gyre develops in a channel, even in the absence of lateral boundaries. The presence of a barotropic gyre in the open latitudes can be explained by comparing experiments with and without a lateral western wall. In a closed-box ocean with a half-Gaussian shelf topography, the western boundary current detaches from the western wall and follows the barotropic geostrophic contours, similar to the solution described by Salmon (1992). The topography acts as an effective wall and supports a frictional boundary layer that persists, even when the lateral western boundary is removed. Ignored by Stommel, the vertical transport of zonal momentum by eddies is the key ingredient that allows the flow to feel the bottom topography and be steered via topographic drag.

Our numerical results suggest an interpretation of the role of topography that differs from recent works that emphasized the importance of ridges in deflecting the zonal flow in reentrant channels and thereby generating bottom form drag (e.g., Thompson and Naveira Garabato 2014; Abernathey and Cessi 2014). In these works, the deflection of the flow is described as a standing Rossby wave, quite different from the gyre circulations described here. The gyres span the whole domain—regardless of the length of the channel—unlike the meanders that are confined to the ridges and suggest that the effect of major topographic ridges is better understood as a global rather than a local constraint. While both standing meanders and gyre circulations probably coexist in the simulations, gyre circulations are likely to dominate in long channels, like the ACC, where the Sverdrup transport generated by the wind stress curl is significant.

The relevance of those dynamics for the real ACC is further supported by two important considerations: First, the time-averaged wind stress has a significant curl, and it is thus capable of generating a substantial meridional Sverdrup transport. Also, all the ACC barotropic geostrophic contours, shown in Fig. 15, are blocked by the major topographic features in the Southern Ocean and can therefore support meridional boundary currents. However, future work will need to explore how to best identify the gyre circulations in the Southern Ocean, where the topography is far more complex than the one used in this study. For example, in the Southern Ocean, the gyre mode may be divided into

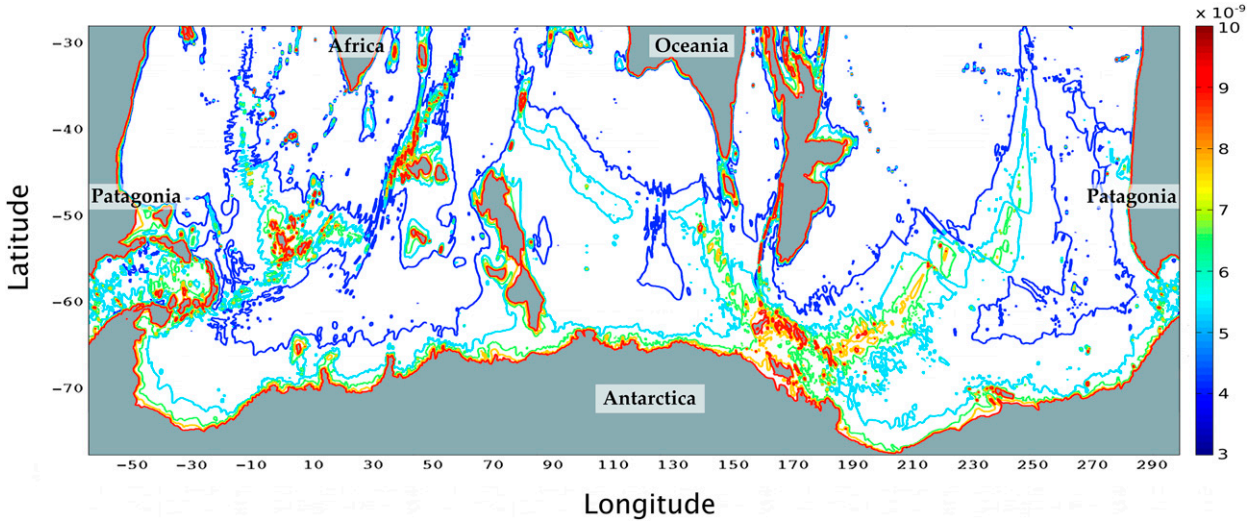

FIG. 15. Contours of f/h in the Southern Ocean shows obtained using ETOPO5. Values higher than $10^{-9}\,\mathrm{s}^{-1}\,\mathrm{m}^{-1}$ have been shaded in gray.

multiple smaller subdomains defined by the major topographic features (Scotia Ridge, Kerguelen Plateau, Southeast Indian Ridge, Campbell Plateau, Pacific Antarctic Ridge, etc.). Figure 9 shows how gyres are harder to identify for smaller channel subdomains. As such, the gyre mode introduced here for a single ridge may be replaced by a "topographic mode" that better reflects the complexity of the Southern Ocean's topography and describe more accurately the convoluted path of the ACC's major meanders. We think that these topographic modes may have important implications for water mass transformations in the Southern Ocean because they may dominate the meridional transports in the ocean abyss.

Finally, our work has shown that the flow in a reentrant channel with topographic ridges can be thought as the superposition of gyre and circumpolar modes. We showed that the transport in the gyre mode is set by the wind stress curl through Sverdrup's relationship, but work is still needed to derive a theory for what sets the strength of the circumpolar transport. It also remains to be verified that our results generalize the presence of a surface thermal forcing, which was ignored in this study.

Acknowledgments. We thank David Straub, Nicolas Grisouard, and David Ferreira for helpful discussions and help with the MITgcm. Thanks to David Holland and the NYU HPC team for the computing facilities at NYU. We acknowledge support from a Mathematics and Climate Research Network (MCRN) fellowship (LPN) and an NSF OCE-1233832 Award (LPN and RF).

APPENDIX

Quasigeostrophic Numerical Model

Following Pedlosky (1996), the quasigeostrophic potential vorticity equations truncated to two layers can be written as

$$D_t(\nabla^2\psi_1 - F_1(\psi_1 - \psi_2) + \beta y - F_0\psi_1) = -A_h\nabla^6\psi_1 + \frac{\hat{k}\cdot\nabla\times\boldsymbol{\tau}}{\rho_1 H_1}, \quad \text{and} \tag{A1}$$

$$D_t\left(\nabla^2\psi_2 + F_2(\psi_1 - \psi_2) + \beta y + \frac{f_0}{H_2}h_b\right) = -A_h\nabla^6\psi_2 - r\nabla^2\psi_2, \tag{A2}$$

where $D_t(\ ) = \partial/\partial t(\ ) + \mathrm{J}[\psi, (\ )]$ is the total time derivative; $F_0 = f_0^2/(gH_1)$; $F_1 = f_0^2/(g'H_1)$; $F_2 = f_0^2/(g'H_2)$; f_0 is the mean Coriolis parameter; β is the northward spatial derivative of the Coriolis parameter; g is the gravitational acceleration; $g' = g(\Delta\rho/\rho)$ is the reduced gravity; H_k are layer thicknesses; h_b is bottom topography; A_h is a lateral biharmonic viscosity coefficient; r is a bottom drag coefficient; and $\boldsymbol{\tau}$ is the wind stress.

Mass conservation is achieved in each layer by imposing

$$\int_0^{L_x}\int_0^{L_y}\psi_k\,dx\,dy = 0. \tag{A3}$$

In the channel configuration, momentum conservation is also taken into account, following a procedure similar to that described by McWilliams et al. (1978), using the zonal momentum equation integrated over a latitude circle in the channel

$$\oint_0^{L_x}\left[D_t(u_{0k}) - f_0 v_{1k} - \beta y v_{0k} = -g\partial_x \eta_1 - \delta_{N,k} r u_{0k} - A_H \nabla^4 u_{0k} + \delta_{1,k}\frac{\tau}{\rho_1 H_1}\right] dx, \tag{A4}$$

where $(u_0, v_0) = (-\partial_y \psi, \partial_x \psi)$ is the horizontal velocity, and $\eta_k = (f_0/g_k)\psi_k$ is the interface height. Note that $\oint_0^{L_x}(\partial_x \eta_1)\, dx$ is zero. The order Rossby number correction to the meridional velocity v_1, is obtained from mass flux conservation across the same latitude circle over which the zonal momentum Eq. (A4) is integrated

$$\oint_0^{L_x}[(H_k v_{1k}) - v_{0k}(\eta_k - \eta_{k-1})]\, dx = \frac{d}{dt}\left[\iint_A (\eta_k - \eta_{k-1})\, dx\, dy\right], \tag{A5}$$

where A is the area south of the latitude where the above integral is taken.

In the box configuration, only Eq. (A3) is used to set the value of ψ at the boundary. In the channel configuration, the set of equation formed by Eqs. (A3) and (A4) is solved to set the values of ψ at the northern and southern boundaries.

REFERENCES

Abernathey, R., and P. Cessi, 2014: Topographic enhancement of eddy efficiency in baroclinic equilibration. *J. Phys. Oceanogr.,* **44,** 2107–2126, doi:10.1175/JPO-D-14-0014.1.

Arakawa, A., 1966: Computational design for long-term numerical integrations of the equations of atmospheric motion. *J. Comput. Phys.,* **1,** 119–143, doi:10.1016/0021-9991(66)90015-5.

Firing, Y., T. Chereskin, and M. Mazloff, 2011: Vertical structure and transport of the Antarctic Circumpolar Current in Drake Passage from direct velocity observations. *J. Geophys. Res.,* **116,** C08015, doi:10.1029/2011JC006999.

Gill, A., 1968: A linear model of the Antarctic Circumpolar Current. *J. Fluid Mech.,* **32,** 465–488, doi:10.1017/S0022112068000868.

Hallberg, R., and A. Gnanadesikan, 2006: The role of eddies in determining the structure and response of the wind-driven Southern Hemisphere overturning: Results from the Modeling Eddies in the Southern Ocean (MESO) project. *J. Phys. Oceanogr.,* **36,** 2232–2252, doi:10.1175/JPO2980.1.

Hill, C., D. Ferreira, J.-M. Campin, J. Marshall, R. Abernathey, and N. Barrier, 2012: Controlling spurious diapycnal mixing in eddy-resolving height-coordinate ocean models: Insights from virtual deliberate tracer release experiments. *Ocean Modell.,* **45-46,** 14–26, doi:10.1016/j.ocemod.2011.12.001.

Hogg, A. M., and J. R. Blundell, 2006: Interdecadal variability of the Southern Ocean. *J. Phys. Oceanogr.,* **36,** 1626–1645, doi:10.1175/JPO2934.1.

Johnson, G. C., and H. Bryden, 1989: On the strength of the circumpolar current. *Deep-Sea Res.,* **36,** 39–53, doi:10.1016/0198-0149(89)90017-4.

Leith, C. E., 1967: Diffusion approximation to inertial energy transfer in isotropic turbulence. *Phys. Fluids,* **10,** 1409–1416, doi:10.1063/1.1762300.

Marshall, J., and T. Radko, 2003: Residual-mean solutions for the Antarctic Circumpolar Current and its associated overturning circulation. *J. Phys. Oceanogr.,* **33,** 2341–2354, doi:10.1175/1520-0485(2003)033<2341:RSFTAC>2.0.CO;2.

——, and K. Speer, 2012: Closure of the meridional overturning circulation through Southern Ocean upwelling. *Nat. Geosci.,* **5,** 171–180, doi:10.1038/ngeo1391.

——, A. Adcroft, C. Hill, L. Perelman, and C. Heisey, 1997a: A finite-volume, incompressible Navier Stokes model for studies of the ocean on parallel computers. *J. Geophys. Res.,* **102,** 5753–5766, doi:10.1029/96JC02775.

——, C. Hill, L. Perelman, and A. Adcroft, 1997b: Hydrostatic, quasi-hydrostatic, and nonhydrostatic ocean modeling. *J. Geophys. Res.,* **102,** 5733–5752, doi:10.1029/96JC02776.

Mazloff, M. R., P. Heimbach, and C. Wunsch, 2010: An eddy-permitting Southern Ocean state estimate. *J. Phys. Oceanogr.,* **40,** 880–899, doi:10.1175/2009JPO4236.1.

McWilliams, J. C., W. R. Holland, and J. H. S. Chow, 1978: A description of numerical Antarctic Circumpolar Currents. *Dyn. Atmos. Oceans,* **2,** 213–291, doi:10.1016/0377-0265(78)90018-0.

Meredith, M., A. Naveira Garabato, A. Hogg, and R. Farneti, 2012: Sensitivity of the overturning circulation in the Southern Ocean to decadal changes in wind forcing. *J. Climate,* **25,** 99–110, doi:10.1175/2011JCLI4204.1.

Morrison, A. K., and A. Hogg, 2013: On the relationship between Southern Ocean overturning and ACC transport. *J. Phys. Oceanogr.,* **43,** 140–148, doi:10.1175/JPO-D-12-057.1.

Munday, D., H. Johnson, and D. Marshall, 2013: Eddy saturation of equilibrated circumpolar currents. *J. Phys. Oceanogr.,* **43,** 507–532, doi:10.1175/JPO-D-12-095.1.

Munk, W., and E. Palmen, 1951: Note on the dynamics of the Antarctic Circumpolar Current. *Tellus,* **3A,** 53–55, doi:10.1111/j.2153-3490.1951.tb00776.x.

Nadeau, L.-P., and D. Straub, 2009: Basin and channel contributions to a model Antarctic Circumpolar Current. *J. Phys. Oceanogr.,* **39,** 986–1002, doi:10.1175/2008JPO4023.1.

——, and ——, 2012: Influence of wind stress, wind stress curl, and bottom friction on the transport of a model Antarctic Circumpolar Current. *J. Phys. Oceanogr.,* **42,** 207–222, doi:10.1175/JPO-D-11-058.1.

——, ——, and D. Holland, 2013: Comparing idealized and complex topographies in quasigeostrophic simulations of an Antarctic Circumpolar Current. *J. Phys. Oceanogr.,* **43,** 1821–1837, doi:10.1175/JPO-D-12-0142.1.

Olbers, D., D. Borowski, C. Voelker, and J.-O. Wolff, 2004: The dynamical balance, transport and circulation of the Antarctic Circumpolar Current. *Antarct. Sci.,* **16,** 439–470, doi:10.1017/S0954102004002251.

Pedlosky, J., 1996: *Ocean Circulation Theory.* Springer, 453 pp.

Prather, M. J., 1986: Numerical advection by conservation of second-order moments. *J. Geophys. Res.,* **91,** 6671–6681, doi:10.1029/JD091iD06p06671.

Salmon, R., 1992: A two-layer Gulf Stream over a continental slope. *J. Mar. Res.,* **50,** 341–365, doi:10.1357/002224092784797610.

Stommel, H., 1948: The westward intensification of wind-driven ocean currents. *Eos, Trans. Amer. Geophys. Union,* **29,** 202–206.

——, 1957: A survey of ocean current theory. *Deep-Sea Res.,* **4,** 149–184, doi:10.1016/0146-6313(56)90048-X.

Straub, D. N., 1993: On the transport and angular momentum balance of channel models of the Antarctic Circumpolar Current. *J. Phys. Oceanogr.,* **23,** 776–782, doi:10.1175/1520-0485(1993)023<0776:OTTAAM>2.0.CO;2.

Tansley, C. E., and D. P. Marshall, 2001: On the dynamics of wind-driven circumpolar currents. *J. Phys. Oceanogr.,* **31,** 3258–3273, doi:10.1175/1520-0485(2001)031<3258:OTDOWD>2.0.CO;2.

Thompson, A. F., and A. C. Naveira Garabato, 2014: Equilibration of the Antarctic Circumpolar Current by standing meanders. *J. Phys. Oceanogr.,* **44,** 1811–1828, doi:10.1175/JPO-D-13-0163.1.

Ward, M., and A. M. Hogg, 2011: Establishment of momentum balance by form stress in a wind-driven channel. *Ocean Modell.,* **40,** 133–146, doi:10.1016/j.ocemod.2011.08.004.

Wunsch, C., and A. E. Gill, 1976: Observations of equatorially trapped waves in Pacific sea level variations. *Deep-Sea Res. Oceanogr. Abstr.,* **23,** 371–390, doi:10.1016/0011-7471(76)90835-4.